Cell Calcium 86 (2020) 102152

Contents lists available at ScienceDirect

Cell Calcium

journal homepage: www.elsevier.com/locate/ceca

Noise analysis of cytosolic calcium image data

Divya Swaminathan[a,*], George D. Dickinson[a], Angelo Demuro[a], Ian Parker[a,b]

[a] Department of Neurobiology & Behavior, University of California, Irvine, CA92697, USA
[b] Department of Physiology & Biophysics, University of California, Irvine, CA92697, USA

ARTICLE INFO

Keywords:
Ca^{2+} imaging
Ca^{2+} puffs
Ca^{2+} noise
Noise analysis

ABSTRACT

Cellular Ca^{2+} signals are often constrained to cytosolic micro- or nano-domains where stochastic openings of Ca^{2+} channels cause large fluctuations in local Ca^{2+} concentration (Ca^{2+} 'noise'). With the advent of TIRF microscopy to image the fluorescence of Ca^{2+}-sensitive probes from attoliter volumes it has become possible to directly monitor these signals, which closely track the gating of plasmalemmal and ER Ca^{2+}-permeable channels. Nevertheless, it is likely that many physiologically important Ca^{2+} signals are too small to resolve as discrete events in fluorescence recordings. By analogy with noise analysis of electrophysiological data, we explore here the use of statistical approaches to detect and analyze such Ca^{2+} noise in images obtained using Ca^{2+}-sensitive indicator dyes. We describe two techniques - power spectrum analysis and spatio-temporal correlation - and demonstrate that both effectively identify discrete, spatially localized calcium release events (Ca^{2+} puffs). Moreover, we show they are able to detect localized noise fluctuations in a case where discrete events cannot directly be resolved.

1. Introduction

Ca^{2+} ions serve enormously diverse signaling functions in almost every cell of the body [1,2]. Much of the versatility and specificity of cytosolic Ca^{2+} signals derives from the fact that they can be highly localized in both space and time; a consequence of the rapid flux of Ca^{2+} through channels in the plasma and endoplasmic reticulum (ER) membranes [1,2] and its subsequent constrained diffusion in the face of cytosolic buffers [3–5] and possible physical confinement within cellular microdomains [6]. A consequence of the minute size of relevant sub-cellular volumes is that stochastic variations in local Ca^{2+} concentration become appreciable. For example, a 1 µm cube of cytosol (1 fL; 10^{-15} L volume) at a basal free [Ca^{2+}] of 100 nM contains on average just 60 free ions. From binomial statistics the standard deviation of fluctuations around this mean is about 8 Ca^{2+} ions. Beyond this, much larger fluctuations will arise in small cytosolic volumes around Ca^{2+} channels as they stochastically open and close [7,8]. Thus, the localized changes in [Ca^{2+}] that play vital roles in modulating the activity of ion channels, buffers, enzymes and other proteins [1,2] cannot be understood simply in deterministic terms of average concentrations. Instead, we must take into account the stochastic, spatially inhomogeneous temporal fluctuations in local Ca^{2+} concentration. Here, we describe our efforts to detect and analyze such Ca^{2+} 'noise 'from live cell imaging data.

Minimally invasive optical imaging techniques, in conjunction with Ca^{2+}-specific fluorescent indicator dyes, provide a sensitive means to measure and visualize Ca^{2+} elevations with sub-cellular resolution. The advent of total internal reflection fluorescence (TIRF) microscopy has considerably improved the resolution of local [Ca^{2+}] signals as compared to conventional wide-field or confocal fluorescence microscopy: the critical difference being the volume from which fluorescence of a Ca^{2+} indicator dye is collected. The magnitude of stochastic free Ca^{2+} fluctuations relative to the mean is inversely proportional to the square root of volume [9], and fluctuations arising from gating of a single Ca^{2+} channel increase in amplitude and kinetic resolution of channel gating as the cytosolic volume around the pore from which fluorescence is measured is reduced. Indeed, in a detailed computational study, Shuai & Parker [10] found that optimal kinetic resolution could be expected only by monitoring fluorescence from sampling volumes of 0.1 fL or smaller. Recordings over larger volumes, as in wide-field fluorescence microscopy, average out fluctuations in the Ca^{2+} signal and fail to resolve Ca^{2+} flux through individual channels. TIRF microscopy is a near-field imaging technique where fluorescence excitation (the evanescent wave) is confined to an exponentially decaying (~ 100 nm) field adjacent to the cover glass [11]. The lateral (x–y) resolution in this optical plane is about 400 nm, so that fluorescence can be monitored from regions of interest encompassing attoliter (400 × 400 × 100 nm = 16 aL) volumes around channels located within the evanescent field.

---

[*] Corresponding author at: 1146 McGaugh Hall, University of California, Irvine, CA, 92697, USA.
E-mail address: dswamina@uci.edu (D. Swaminathan).

https://doi.org/10.1016/j.ceca.2019.102152
Received 13 August 2019; Received in revised form 15 December 2019; Accepted 16 December 2019

We have previously used TIRF microscopy to image Ca^{2+} fluorescence transients arising from single voltage- and ligand-gated Ca^{2+}-permeable channels [12,13] and to dissect the individual contributions of tightly clustered inositol trisphosphate receptor/channels (IP_3Rs) in the ER membrane during localized Ca^{2+} release events (Ca^{2+} puffs) [14]. Our goal here was to develop generalized approaches to analyze local Ca^{2+} fluctuations in TIRF imaging data, with the aims of improving detection of single-channel Ca^{2+} signals and determining whether fluctuation analysis may reveal information about biologically important signals that are otherwise too small to directly resolve.

To test and apply our computational approaches we continued to use the IP_3R as a well-characterized model system for Ca^{2+} imaging. The IP_3R is a Ca^{2+}-permeable channel in the ER membrane, responsible for liberation of Ca^{2+} into the cytosol in response to binding of IP_3 and cytosolic Ca^{2+} itself [1]. Co-activation by Ca^{2+} imparts a property of Ca^{2+}-induced Ca^{2+} release (CICR), such that Ca^{2+} flux through one IP_3R promotes the opening of neighboring channels. This potentially regenerative process is constrained by the cellular organization of functional IP_3Rs into stable clusters of several channels [15,16], so that stimulation of IP_3 signaling may evoke Ca^{2+} release from individual channels evoking fluorescence signals called blips [17], or the concerted opening of multiple channels in a cluster to generate a larger Ca^{2+} puff [14]. Blips and puffs can be directly resolved as discrete events in TIRF images and thus serve as a useful control to demonstrate the effective use of power spectra and correlations in identifying active Ca^{2+} release sites and characterizing single-channel release events within cells. Further, we explore the use of these techniques to identify local IP_3-mediated Ca^{2+} signals that are too small to resolve directly as discrete events

2. Development of analytical methods

In this section we lay out the conceptual principles we use to analyze Ca^{2+} fluctuations – identifying potential noise sources in fluorescence images, and introducing the power spectra and cross-correlation techniques we apply.

2.1. Noise sources in fluorescence Ca^{2+} imaging

We begin by considering potential sources and characteristics of fluorescence fluctuations arising from small cytosolic volumes as imaged by TIRF microscopy.

(i) 'Instrumental noise': This includes fluctuations from sources including variations in laser power or pointing stability, camera gain, and mechanical vibration which are expected to be uniform over the entire imaging field; and sources such as camera dark noise that are uncorrelated between different camera pixels.

(ii) 'Photon shot noise': stochastic fluctuations in the number of photons collected per pixel per unit time. For photon shot noise, the variance (power) increases linearly with the mean number of photons (intensity) and is uncorrelated across different pixels.

(iii) 'Molecular shot noise': Statistical fluctuations in the numbers of Ca^{2+}-bound indicator molecules within a local volume. These fluctuations arise due to binding/unbinding kinetics of Ca^{2+} to the dye, diffusion of free and indicator-bound Ca^{2+} molecules in and out of the local volume, and binding and unbinding of Ca^{2+} ions to cellular buffers. Because of optical blurring fluctuations may be correlated across a few adjacent camera pixels, corresponding to distances of a few hundred nm in the specimen.

(iv) 'Ca^{2+} channel noise': Fluctuations in the total number of Ca^{2+} ions within a local cytosolic volume resulting from flux through stochastic gating of Ca^{2+} channels. In the case of rapid binding and unbinding to the indicator the fluctuations in fluorescence will approximately track fluctuations in local free [Ca^{2+}]. These fluctuations may be temporally correlated across several hundred nm in the specimen owing to the rapid diffusion of Ca^{2+} ions and Ca^{2+}-bound indicator molecules over this short distance scale.

We present here computational tools to detect and analyze Ca^{2+} channel noise. Inherently, this will be present together with the other noise sources listed above. With the exception of instrumental noise, these sources cannot be mitigated; instead we seek to identify and measure them based on their different characteristics, so they may be subtracted from the total noise variance to reveal that component resulting from channel noise. Drawing inspiration from Katz and Miledi's seminal study on electrophysiological recordings of endplate noise [18], we applied two techniques - power spectrum and spatio-temporal correlation analysis - to identify and characterize noise fluctuations in Ca^{2+} imaging data obtained using TIRF microscopy.

2.2. Power spectrum analysis

The Power Spectrum or spectral density function S(f) of a time trace describes how power (variance) of the data is distributed in the frequency domain, and is a powerful tool for recognizing signals or periodicities in underlying data. Power spectra have been extensively applied to electrophysiological data to analyze underlying channel properties [18–20]. We extend this approach to fluorescence image sequences obtained by TIRF microscopy. We first consider spectral analysis of individual, sub-femtoliter volumes of interest, and then describe the spatial mapping of multiple spectra across the x–y imaging plane.

A primary motivation for undertaking power spectrum analysis is to discriminate among the four noise sources listed above. As a function of fluorescence excitation intensity we expect that the total noise power (variance) of instrumental noise sources such as laser power fluctuations will increase as the square of intensity, but be independent of sources such as dark noise of camera pixels; that photon shot noise will increase as a linear function of intensity; and that both molecular shot noise and Ca^{2+} channel noise will increase as the square of intensity. A further discrimination between these noise sources is possible by considering their spectra, as reflecting the kinetics of the underlying processes generating the fluctuations. The spectrum of instrumental noise is unknown but in our recordings we find it can be ignored as negligible. Photon shot noise is equal at all frequencies ('white' noise), yielding a flat spectrum across the bandwidth of the recording system. The kinetics of molecular shot noise are governed by binding/unbinding of Ca^{2+} ions to indicator dye, and the diffusion of these entities. These are both fast processes so we expect the spectrum of molecular shot noise to roll off at frequencies that will typically be higher than expected from Ca^{2+} channel noise.

In our experiments the camera frame rate ranges between $125-500$ Hz. A single pixel encompasses 333 nm at the specimen and the associated TIRF volume, calculated using eq.11 from [10], is approximately 14 aL. For a diffusion coefficient of 200 $\mu m^2 s^{-1}$ (approximately that expected for free Ca^{2+} and Ca^{2+} indicator) the cutoff frequency within this volume (purely due to diffusion) is predicted to be about 555 Hz. Thus, the spectrum of molecular shot noise would appear flat within the bandwidth of our recordings. Different to this, membrane channels typically gate with mean open times in the millisecond range. For a channel alternating between open and closed states, the resulting spectrum of ion flux through the channel is a Lorentzian function of frequency with a cutoff (half-power frequency) given by $fc = 1/(2\pi\tau)$ where τ is a measure of the mean channel open and close times as $\tau = \tau_{on}\tau_{off}/(\tau_{on} + \tau_{off})$ [19]. Under conditions of low open probability ($\tau_{off} \gg \tau_{on}$) the cut off frequency of the spectra then provides a measure of mean channel open time. In terms of local Ca^{2+}-dependent fluorescence signals we therefore expect that the spectrum generated by an actively gating Ca^{2+} channel will primarily show a Lorentzian with cutoff frequency determined by channel kinetics and this spectrum, for a given volume, would typically have a lower cut off frequency than molecular shot noise.

2.3. The power spectrum map

We construct a 2D ‘power spectrum map’ (PSM) by implementing the power spectra analysis on 3D fluorescence image sequences. Local fluorescence transients arising from channel activity are expected to show most power at low frequencies, superimposed on a flat spectrum of photon and molecular shot noise. To isolate the component resulting from Ca^{2+} fluctuations we thus calculate the difference between power averaged over a low frequency range $< P_{LFR} >$ (typically $0.1 < f < = 5$ Hz) and power averaged over a high frequency range $< P_{HFR} >$ ($f > 50$ Hz). By mapping the numerical value of this difference for all spatial coordinates we generate a pictorial representation of regions exhibiting transient local Ca^{2+}release.

2.4. Spatio-temporal correlation analysis

In addition to differences in their frequency spectra, we further expect that the various noise sources will differ in the extent to which fluctuations are correlated both in time and in space across the imaging field. For any given pixel we thus cross-correlate the fluorescence time trace at that pixel with fluorescence traces from neighboring pixels at varying distances. Photon shot noise is independent for each pixel, so the cross correlation is expected to result in zero average value. For molecular shot noise a small correlation may be expected between closely adjacent pixels, because light emitted by a given indicator molecule would be blurred across the camera sensor by the point-spread function of the microscope optics. However, any temporal correlation would be present at only very short lags given the rapid kinetics of molecular shot noise. Different from this, fluorescence transients arising from Ca^{2+} flux through channels will typically persist for longer times and spread over wider spatial extents due to diffusion of the Ca^{2+}-dye complex in the cytosol.

Different from the power spectra calculations that consider only temporal data, the cross correlation calculations take into account both the spatial and temporal characteristics of imaged data.

2.5. The correlation map

We visualize spatio-temporal correlations within the 3D fluorescence image stacks by constructing a 2D ‘correlation map’ (CRM). Analogous to the PSM, the CRM is a pictorial representation of local, spatially and temporally correlated Ca^{2+} fluorescence activity. To construct a correlation map we cross-correlate the fluorescence trace of each pixel with fluorescence traces from its eight nearest neighbors and sum the resultant averaged cross-correlation up to a specified time lag. This summed averaged correlation value is the numeric value associated with each pixel in the correlation map. The choice of time lag is chosen to be neither too small as to pick up spurious molecular shot noise spatial correlations due to optical blurring nor too long as to decrease the cross correlation value from a local Ca^{2+} release event.

3. Methods

3.1. Cell culture and imaging

Ca^{2+} image data were obtained from two cell types; cultured SH-SY5Y neuroblastoma cells, and *Xenopus* oocytes.

SH-SY5Y cells were cultured and loaded for imaging using membrane permeant esters of fluo 4, EGTA and caged i-IP_3 (c-iIP_3) as described [21]. A single flash of UV light (350–400 nm) from an arc lamp focused to uniformly illuminate a region slightly larger than the imaging frame was used to uncage i-IP_3, a metabolically stable isopropylidene analog of IP_3, which evoked activity persisting for a few minutes [21].

Stage V-VI *Xenopus laevis* oocytes were purchased from Ecocyte Bioscience International (Austin, Texas) and prepared for imaging as described [22]. About an hour prior to $[Ca^{2+}]_i$ imaging, oocytes in Ca^{2+}-free Barth’s solution were injected with low affinity fluo-4 dextran (K_d for Ca^{2+} ∼ 3 μM) to a final concentration of 40μM, assuming even distribution throughout a 1 μl cytosolic volume [22]. Microinjection of IP_3 into oocytes during imaging was performed using a Drummond nanoinjector mounted vertically on a hydraulic micromanipulator affixed to the microscope frame. A glass pipette filled with IP_3 solution was inserted vertically down through the entire oocyte to a pre-established position, with the tip positioned a few μm inward from the plasma membrane and centered within the image field [22]. 10 μl of 100 pM IP_3 was injected into the oocytes.

For both cell types, $[Ca^{2+}]_i$ changes were imaged using TIRF microscope systems constructed around Olympus IX 70 microscopes (Olympus, Center Valley, PA) with a 60 X TIRF objective (NA,1.45) as described [21]. Fluo-4 fluorescence was excited by 488 nm laser light within an evanescent field extending a few hundred nanometers into the cells, and emitted fluorescence was imaged at ($\lambda > 510$ nm) at a resolution of 128 × 128 pixels (1 pixel = 333 nm) using a Cascade 128 electron-multiplied ccd camera (Roper Scientific, Tucson, Az) at a frame rate of 125 s^{-1} for SH-SY5Y cells and 500 s^{-1} for oocytes. Image data were acquired as stack files using MetaMorph v 7.7 (Universal Imaging/ Molecular Devices, Sunnyvale, CA) for offline analysis using MetaMorph [21].

3.2. Computational analysis

All raw image stacks obtained in (x,y,T) format from experiments were processed using custom Matlab codes to calculate power spectra and correlation maps. All codes were written using Matlab (R2011b; The Mathworks, Inc., Natick, Massachusetts, United States), and are available on request.

4. Results

We illustrate here the application of power spectrum and cross correlation techniques to analyze Ca^{2+} noise in representative live cell TIRF imaging data obtained from SH-SY5Y cells and *Xenopus* oocytes. We first validate these approaches in studying local Ca^{2+} puffs in SH-SY5Y cells, and then apply them to Ca^{2+} signals evoked in oocytes by picoMolar concentrations of IP_3 where localized transients cannot be discerned by conventional analysis.

4.1. Power spectra of Ca^{2+} fluorescence fluctuations

Local Ca^{2+} puffs were imaged in TIRF using SH-SY5Y cells loaded with fluo4, caged i-IP_3 and the slow Ca^{2+} buffer EGTA [21,23]. A long baseline (∼ 5000 frames; 125 frames s^{-1}) was recorded, and a further 6000 frames following photorelease of i-IP_3.

Fig. 1 illustrates the calculation of power spectra from a 3 × 3 pixel region of interest (ROI) positioned at a local Ca^{2+} puff site. A Matlab filter ‘Sgolayfilt’ was applied to the fluorescence time traces (upper gray traces in Fig. 1A) to strip any gradual increase in basal fluorescence (lower colored traces). Filtered traces at baseline are shown in blue, and following photorelease of i-IP_3 in red. Traces were then sub-sectioned in time, and Fig. 1 B, C show representative sections (1024 frames each) on an expanded scale. Power spectra for all sections were calculated using fast Fourier transforms, and the mean spectra are plotted in Fig. 1D for 4 baseline sub-sections and Fig. 1E for 5 sub-sections during which puffs were evoked. Because power spectra were calculated from raw fluorescence traces, power is reported in arbitrary units, representing the variation in recorded intensity per unit frequency. Comparing the two spectra, the baseline is flat (Fig. 1D), whereas the spectrum in the presence of Ca^{2+} puffs (Fig. 1E) shows an excess of low frequency power, decreasing to the shot noise-dominated floor at high frequencies.

For every individual averaged spectrum, three quantities were

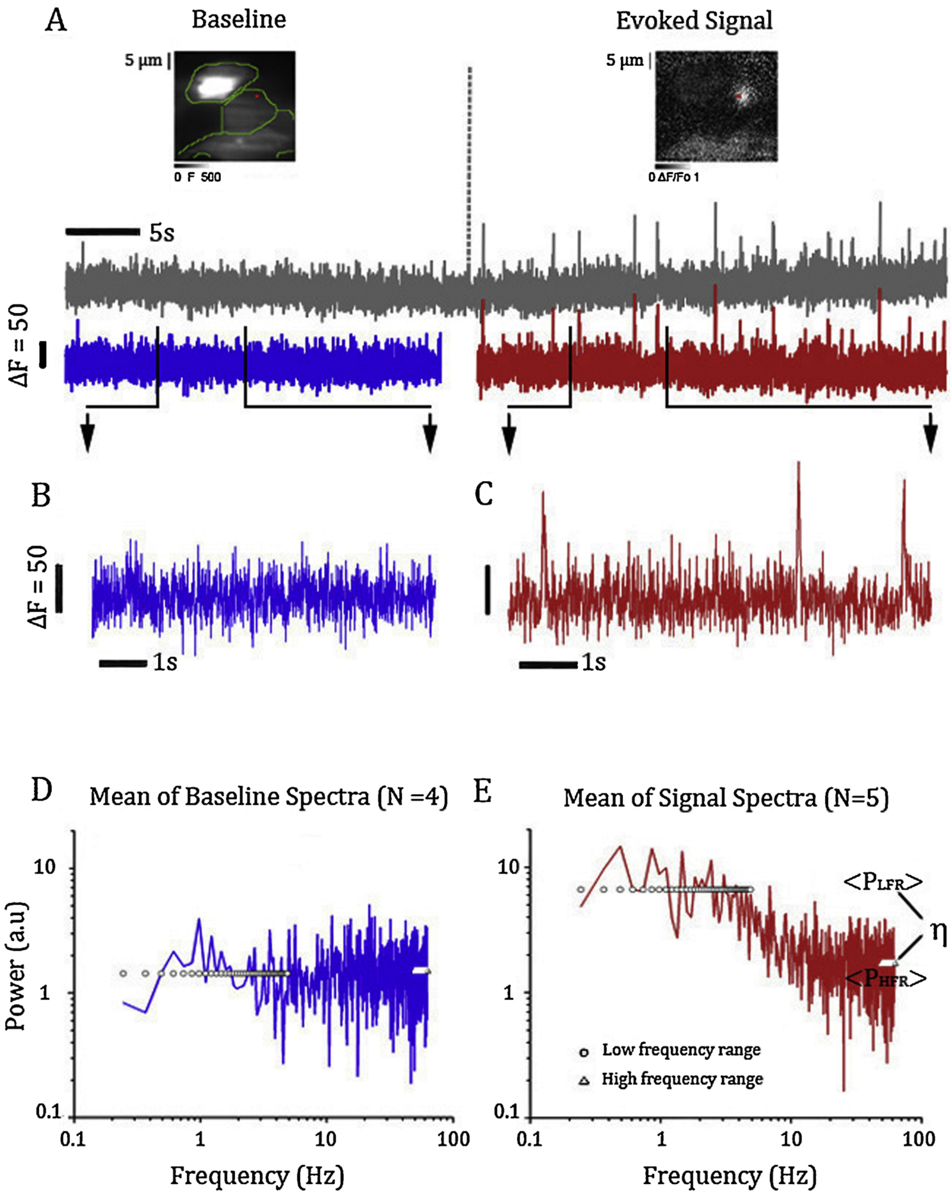

Fig. 1. Calculation of power spectra from fluorescence at a single 3 × 3 pixel ROI. (A) Image panels show the raw fluorescence image of a field containing three SH-SY5Y cells (outlined in green) at rest, and a $\Delta F/F_o$ ratio image illustrating a Ca^{2+} puff evoked after photorelease of i-IP_3 (right). The red spot marks the 3 × 3pixel ROI from which records were obtained. The gray trace shows fluorescence measured from the ROI centered on the puff site before and after photorelease of i-IP_3 (when indicated by dotted line). Colored traces were derived by stripping gradual changes in fluorescence using a Sgolayfilt filter. (B, C) Individual time sub-sections (1024 frames) from baseline and signal traces, respectively, shown on an expanded scale. (D, E) Plots show respective mean power spectra from 4 baseline sub-sections, and 5 sub-sections after photorelease of i-IP_3. Circles mark averaged power over a low (0.1 − 5 Hz) frequency range (P_{LFR}), and triangles mark averaged power over a high (50 − 62 Hz) frequency range (P_{HFR}). The excess power ratio η is calculated as (P_{LFR}-P_{HFR})/P_{HFR}. In D, η = -0.05, and in E η = 2.88.

calculated; mean power over a low (0.1 − 5 Hz) frequency range (P_{LFR}), mean power over a high (50 − 62 Hz) frequency range (P_{HFR}), and normalized excess power ratio (η), defined as $\eta = (P_{LFR}\text{-}P_{HFR})/P_{HFR}$. The high frequency power is dominated by photon shot noise, and is thus linearly proportional to fluorescence intensity. By dividing the excess low frequency power by P_{HFR} we thus normalize η for variations in basal fluorescence that may result from factors such as differences in dye loading and regional variations across the cell.

Because photon and molecular shot noise are uncorrelated across adjacent pixels whereas Ca^{2+} fluorescence fluctuations are correlated across a distance set by diffusion in the cytosol, we averaged fluorescence signals over several pixels within a ROI before calculating power spectra. Fig. 2 illustrates the effect of increased spatial averaging of fluorescence at a ROI centered on a puff site (left panels A–D) and the corresponding spectra (right panels A–D). The choice of area over which to average is a compromise: shot noise is averaged in proportion to the area, whereas the Ca^{2+} signal diminishes as the ROI area is increased beyond the extent of its diffusional spread. Thus, the excess power ratio η increases with increasing area of ROI, but to a diminishing extent with larger areas (right hand panels Fig.2 A–D). The reduced noise in power spectra from larger ROIs enables more accurate fitting of Lorentzian functions to the data (red curves in Fig. 2A–D), which we use to characterize puff kinetics as described in section 4.4. Although by taking a ratio, η normalizes for differences in basal fluorescence, we note that values of η can only be directly compared for ROIs of the same size.

4.2. Power spectrum maps identify active puff sites

To create a spatial map visualizing differences in Ca^{2+}-dependent fluctuations across the imaging field we generate power spectrum maps (PSMs), representing η values on a pseudocolor scale. Fig. 3 illustrates the procedure, applied to an image stack acquired before and after photorelease of i-IP_3 in SH-SY5Y cells (Fig. 3A) to evoke Ca^{2+} puffs. We chose to calculate η values after sub-sampling over ROIs of 3 × 3 camera pixels to generate frames with final dimensions of 42 × 42 pixels. Although larger areas would yield higher values of η they would result in a coarser mapping, and a 3 × 3 pixel ROI gave a sufficient reduction in noise to allow us to detect small Ca^{2+} fluctuations. No Ca^{2+} puffs were evident in the fluorescence records prior to i-IP_3 release, and values of η were near zero across PSMs generated from time sub-sections during this baseline period (Fig. 3B). Following i-IP_3

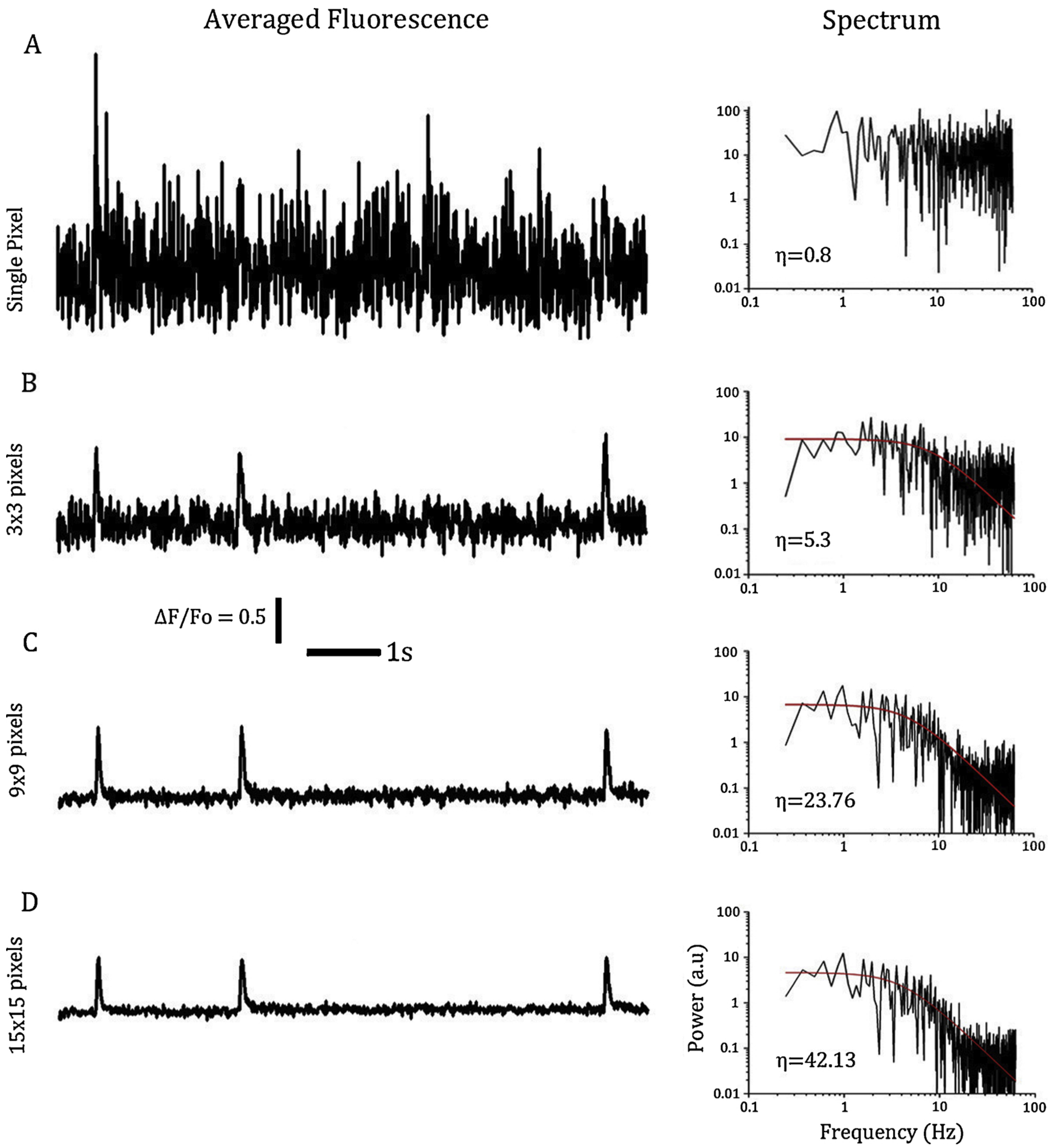

Fig. 2. High frequency shot noise diminishes with increasing spatial averaging of fluorescence, leading to an increase in excess power ratio, η. (A) The trace on the left shows fluorescence monitored from a single pixel centered on a puff site, and the plot on the right shows the power spectrum obtained from this trace. (B–D) Corresponding fluorescence traces and power spectra obtained from progressively larger regions of interest (respectively, 3 × 3, 9x9, and 15x15 pixel ROIs) centered on the same puff site. Respective values of excess power ratio η are indicated, and red curves show Lorentzian functions fitted to the data over all frequencies.

release recurrent puffs arose at several locations in the cells, and PSMs from time subsections showed “hot spots” (Fig. 3C,D; left panels) at locations corresponding to active puff sites in the fluorescence images (Fig. 3C,D; traces on right).

Hot spots showing greater η values corresponded to sites that exhibited larger and/or more frequent puffs in the raw fluorescence record (e.g. compare sites P4 and P3 in the PSM of Fig. 3C). The magnitude of η is more strongly dominated by the amplitude of individual Ca^{2+} events than by their frequency, because excess low frequency power from a puff is proportional to the square of its amplitude but scales about linearly with puff frequency. For example, a single large puff at a site would generate an η value about 10- times greater than that of ten smaller amplitude puffs that together release an equivalent amount of Ca^{2+} over the same time period.

4.3. Mean and maximum power spectrum maps

To visualize cumulative activity over multiple time sub-sections we generate maps depicting either an average of PSMs across individual time-subsections (Fig. 3E), or the maximum η value observed in the PSM for any sub-section (Fig. 3F).

The mean and maximum PSMs highlight different features of underlying puff sites. As noted, the amplitude of a discrete Ca^{2+} signal weights more strongly in the η value than does the frequency of events. Thus, the maximum PSM will tend to be dominated by large events, even if they arise with low frequency and occur even in only a single time sub-section. In the mean PSM on the other hand, the contribution of infrequent events will be diluted, and the η values will be more representative of the cumulative Ca^{2+} activity over the entire recording period.

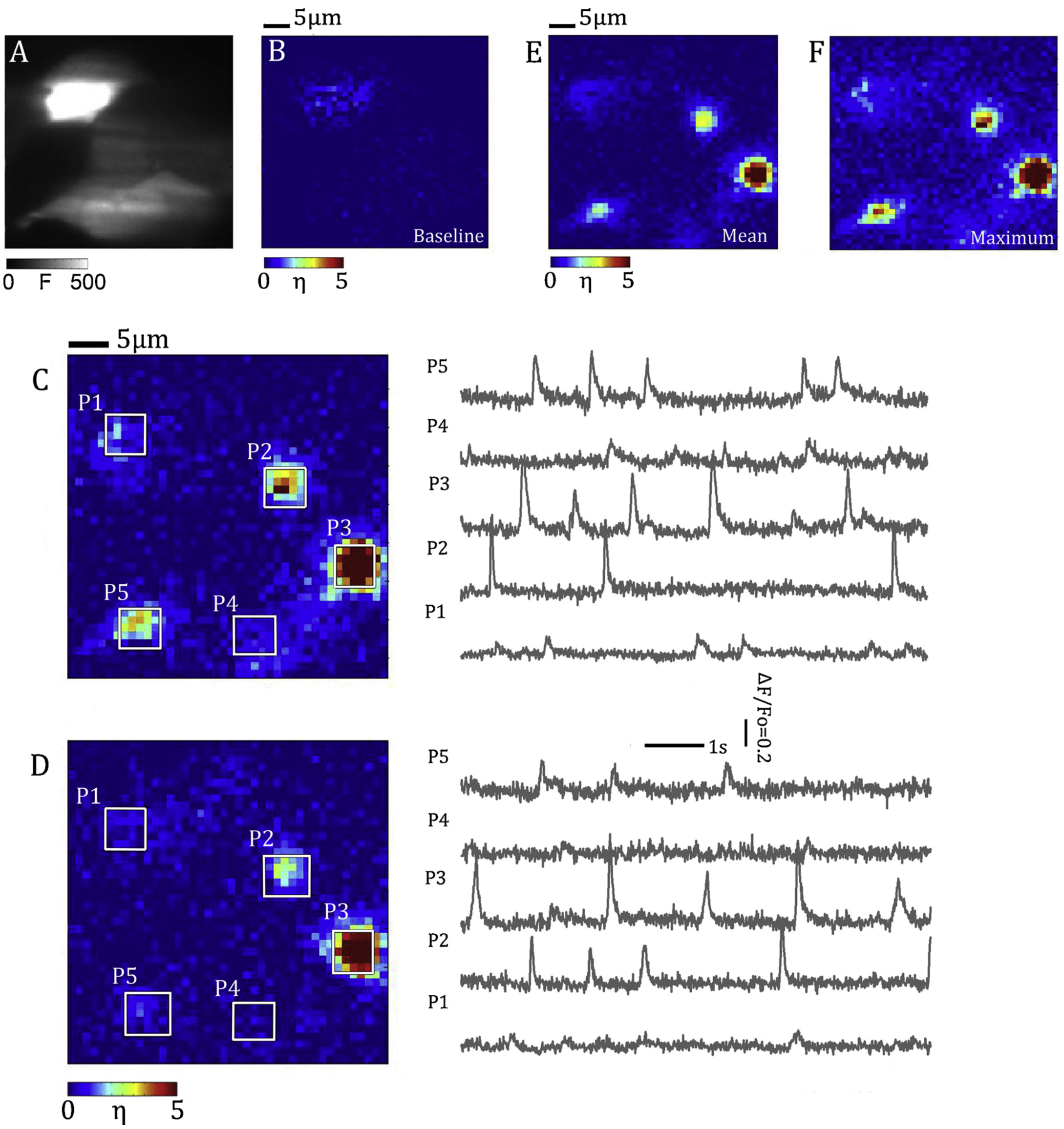

Fig. 3. Power spectrum maps (PSMs) identify 'hot-spots' of puff activity. (A) Raw fluorescence image of the same SH-SY5 cells at baseline, as in Fig. 1A. (B) PSM of these cells generated from a single baseline time sub-section before photorelease of i-IP$_3$. Values of η are depicted on a pseudocolor scale, as indicated by the color bar. (C) PSM for a single time sub-section following i-IP$_3$ release, showing hot-spots of excess power. White boxes mark 5, 15 × 15 pixel, ROIs (P1-P5) centered on these hot-spots, and corresponding traces on the right show average fluorescence measured from these ROIs during the time sub-section. (D) PSM and fluorescence traces for another time sub-section following i-IP$_3$ release. (E) Mean PSM averaged from 5 sub-sections following photorelease of i-IP$_3$. (F) Corresponding maximum PSM derived from the same sub-sections.

This is evident as we compare the mean PSM of Fig. 3E to the maximum PSM of Fig. 3F: all five sites have lower η values in the average when compared to the maximum PSM. Site P1 is hard to identify in the mean PSM (Fig. 3D) but clearly stands out in the maximum PSM (Fig. 3E)). Compared to other sites P1 has lower amplitude puffs hence low η values. In the mean PSM the η value gets diluted whereas the maximum PSM emphasizes single time subsection where the maximum amplitude puff occurred.

4.4. *Characterization of puff kinetics using Lorentzian fits to power spectra*

Ca^{2+} puffs decay approximately as a single exponential, leading to a Lorentzian spectrum where the cut-off frequency at half-maximum power (fc) corresponds to the exponential decay time constant $\tau_{fc} = (2\pi fc)^{-1}$. We can thus derive information about the mean kinetics of local Ca^{2+} signals by fitting Lorentzian functions to power spectra.

For PSMs we calculate η over 3 × 3 pixel ROIs, but for characterization of puff kinetics we averaged fluorescence over 15 × 15 pixel ROIs to reduce photon shot noise and hence allow better fitting of Lorentzian fits to the spectra (Fig. 2). Fig. 4A shows the averaged baseline, signal and difference spectra for the site labeled P2 in Fig. 3B. The baseline spectrum is plotted is blue and is nearly flat. The presence of Ca^{2+} puffs manifests as a low frequency power increase ($f < 10$ Hz) in the spectrum, decaying close to the noise floor at high frequencies (in red). The difference spectrum, in green, plots the absolute increase in power resulting from Ca^{2+} puffs. A Lorentzian function fit (using the built-in Matlab function 'fit') to the difference spectrum (black curve) has a cutoff frequency, fc = 3.7 Hz corresponding to a τ_{fc} = 43 ms. To compare values of puff decay times derived from power spectra with the direct measurements of the time course of fluorescence signals from traces like that in Fig. 2D, we measured the times it took for individual puffs to decay by a factor of 1/e from their peak (τ_{puff}). For example, at site P2, the mean decay time measured from fluorescence records of puffs was 50 ± 3 ms (n = 32 puffs), slightly longer than that (43 ms)

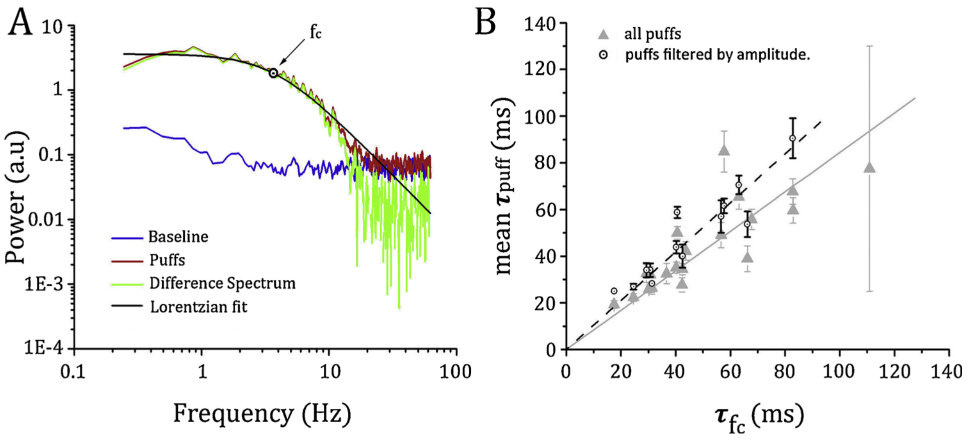

Fig. 4. Determination of puff kinetics from Lorentzian fits to power spectra. (A) Spectra for Site P2 of Fig. 3, showing the mean baseline spectrum (blue), mean spectrum after evoking puffs (red); and the difference of these spectra (green). A Lorentzian fit, over frequency range 0.1–20 Hz, to the difference spectrum is shown in black, with cutoff frequency fc = 3.7 Hz. (B) Scatter plot of puff decay time constants measured directly from fluorescence records (τ_{puff} ; y axis) against puff decay times derived from the cut-off frequency of Lorenzian fits to the power spectra (τ_{fc}; x axis). Gray triangles represent mean τ_{puff} values averaged over all puffs at a given site : the gray line represents the linear relationship between mean τ_{puff} and τ_{fc} (fit slope = 0.84): black circles represent mean τ_{puff} calculated after discarding small amplitude puffs (< 0.2 ΔF/Fo). Removal of small amplitude puffs increases the slope of the linear fit (black dashed line) to 1.04.

derived from the spectral cutoff frequency.

The gray symbols in Fig. 4B plot mean decay times $\bar{\tau}_{puff}$ at 7 sites (3 cells) measured directly from puffs vs. corresponding measurements derived from the cutoff frequency of Lorentzian fits to difference power spectra τ_{fc}. The data fit reasonably well to a linear relationship (gray continuous line), but with a slope of 0.84: that is to say, estimates of puff decay times by Lorentzian fitting were longer than those obtained by direct measurement of fluorescence traces. We suspected that this discrepancy might arise because of difficulties in accurately determining the fluorescence decay of small puffs, and in fitting Lorenzians to spectra with low power. Accordingly, we obtained a better agreement between $\bar{\tau}_{puff}$ and τ_{fc}, with a slope close to unity (1.04) for the linear fit after excluding small amplitude puffs.

In summary, the PSM offers a viable technique for detecting and localizing subcellular Ca^{2+} activity within a cell. Lorentzian functions provide good fits to the difference spectra from puff sites and their cutoff frequencies characterize the average decay time of puffs at an active site. Puff amplitudes play a more significant role than puff frequencies in governing power values.

4.5. *Cross correlation of Ca^{2+} fluorescence fluctuations*

Spatio-temporal correlations provide a complimentary approach to identify and characterize local Ca^{2+}release events. Photon shot noise is uncorrelated between neighboring pixels, whereas fluctuations resulting from local Ca^{2+} elevations evoked by channel openings will be correlated to an extent determined by the diffusion of Ca^{2+} and Ca^{2+}-bound indicator. On this basis we calculate the statistic of cross correlation for experimental data in order to separate Ca^{2+} channel noise from uncorrelated molecular and photon shot noise.

Fig. 5 illustrates our procedure to determine nearest-neighbor cross-correlations and generate correlation maps, applied to the same experimental data as in Figs. 1, 2. Again, we consider a *baseline* stack before i-IP_3 was photoreleased and a *signal* stack representing changes in [Ca^{2+}] levels after uncaging of i-IP_3. Each stack was divided into subsections of 500 frames (4 s). Fig. 5A shows a $\Delta F/F_0$ image of 30 × 30 pixel region averaged over a seven frame (56 ms) time window during the signal stack where a Ca^{2+} puff was observed. We use this puff site to demonstrate how cross-correlations are calculated for a single pixel over a single time sub-section.

Fluorescence traces from each pixel of a 3 × 3 pixel ROI centered on the puff site are plotted in Fig. 5B; the trace from the center pixel is plotted in black and traces from the neighboring eight pixels in gray. The mean fluorescence trace over the entire 3 × 3 pixel ROI is plotted above in blue. We cross-correlated the fluorescence trace of the center pixel (black) with the fluorescence trace of each neighbor (gray), resulting in eight cross-correlation curves. The first fifty lags (1 lag = 1 camera frame = 8 ms) are plotted in gray in Fig. 5C. The average of these eight cross-correlation curves is plotted in red (Fig. 5C) and is associated to the center pixel. Also plotted, in blue, is the mean cross-correlation trace for the center pixel calculated from a single time subsection of the baseline stack.

The mean cross-correlation of the baseline signal (blue trace, Fig. 5C) hovers around zero across all lags, as expected if uncorrelated photon and molecular shot noise are the only major noise sources present. The cross-correlation trace in the presence of puffs (red trace) is strikingly different, showing a strong correlation at short lags, and decaying over about 20 lags (160 ms) to the baseline. No appreciable correlations exist at longer lags.

We use the first fifty lags of the mean correlation curve to calculate a correlation value (ξ) for the center pixel, representing the area under the cross correlation curve. Let ρ*(n)* represent the cross correlation curve of a pixel where n stands for lags, i.e. ρ*(n)* represents the red (or blue) curve of Fig. 5C, then ξ is given by:

$$\xi(\mathrm{p}) \;= (2^{*}\sum_{n=1}^{25} \rho(n) - \sum_{n=1}^{50} \rho(n)) \tag{1}$$

4.6. *Correlation maps (CRMs) identify puff sites*

Repeating this process for every time sub-section, we calculate ξ values for each pixel to generate a 2D pseudo-color map of correlations. Fig. 5D & E show the correlation maps (CRMs) for individual baseline and signal sub-sections. ξ values are near zero throughout the entire baseline field, whereas high, spatially clustered ξ values in the signal sub-section correspond to active puff sites as mapped by the PSMs of Fig. 3. As for PSMs, we construct mean and maximum correlation maps for the signal stack. The maximum correlation map (Fig. 5F) reveals the same sites (P1-P5) as identified in the corresponding PSM map of Fig. 3F. Note that sites P2, P3 & P5, with larger amplitude puffs, have higher correlations as compared to sites P1 & P4 where puff amplitudes are smaller. Larger amplitude puffs have a larger spatial spread, as is also visible in Fig. 5F by the greater extent over which correlations are present.

Owing to the pixel-based mapping of our methodology the CRMs have more visual details when compared to the PSMs which map larger ROIs, although fundamentally both techniques capture the same features of local puffs.

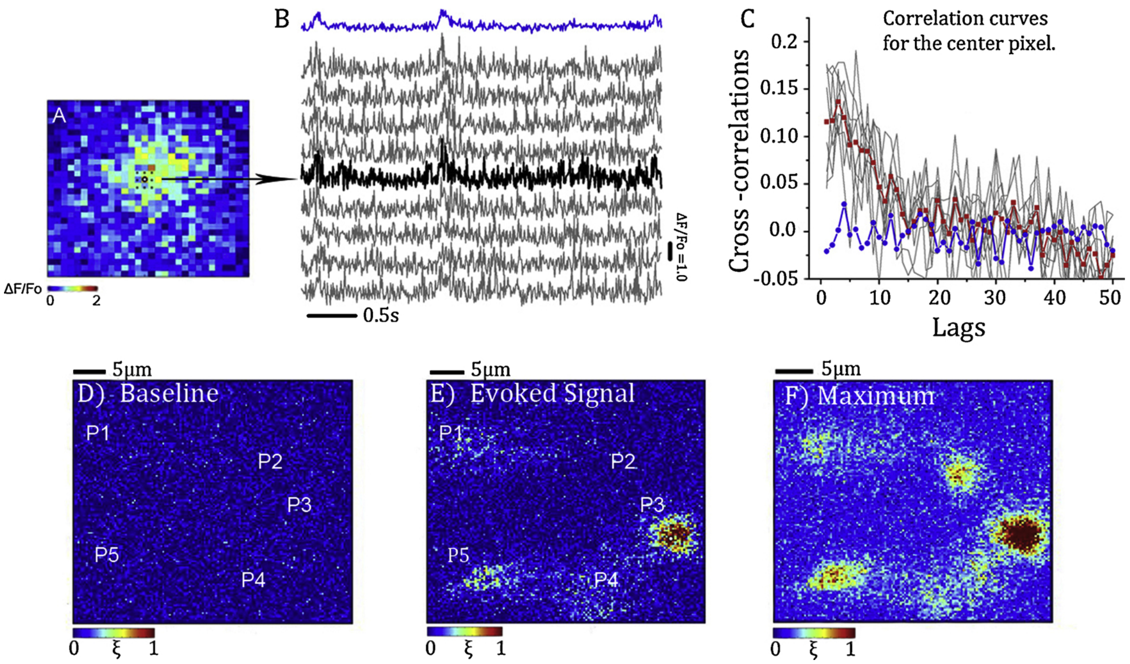

Fig. 5. Spatio-temporal cross-correlations and cross-correlation maps (CRMs). Panels illustrate processing of a single, 500 frame time sub-section following photorelease of i-IP_3. (A) Ratio ($\Delta F/F_0$) image of a puff averaged over seven frames. A single 3 × 3 pixel ROI, centered on this puff site is outlined in white. (B) Fluorescence traces from the center pixel of the ROI (black), from the 8 surrounding pixels (gray), and the mean of all 9 pixels (blue). (C) The red trace shows the mean cross-correlation of center pixel (black trace in B) with its eight neighbors across 50 lags (frames; 1 lag = 8 ms). Individual correlations between the center pixel and each surrounding each pixel are shown in gray. The blue trace shows the mean baseline cross-correlation for the same ROI before uncaging of i-IP_3. The mean cross correlation over the first fifty lags is used to calculate a value of ξ, representing how correlated a given center pixel is to its nearest neighbors. Repeating this process for every pixel across the image field- yields a 2D cross-correlation map representing ξ values. (D, E) Cross-correlation maps derived, respectively, from a single time sub-section before photorelease of i-IP_3 and from a single time sub-section when puffs occurred following photorelease of i-IP_3. (F) Maximum Correlation Map for the signal stack. Data are from the same image stack as illustrated in Fig. 3.

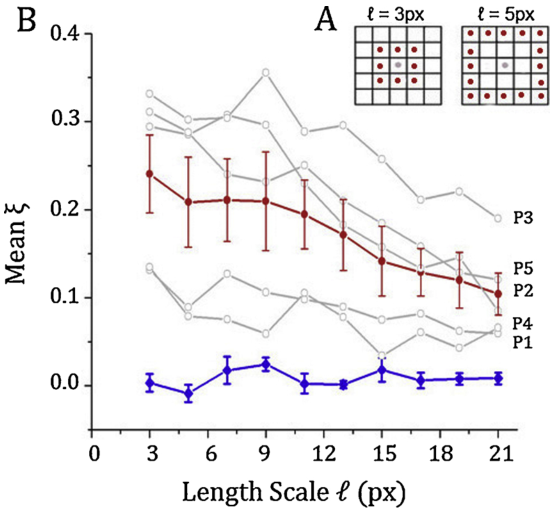

Fig. 6. Spatial extent of cross-correlations. (A) The schematics illustrate calculation of 'ring' correlation ξ values between a center pixel (gray dot) and neighboring peripheral pixels (red dots) at different distances, using 3 × 3 and 5 × 5 pixel regions as examples. (B) The plot shows cross-correlation data derived from the 5 puff sites in 3,5, averaged over 10 time sub-sections. Gray symbols and curves indicate for each individual puff site the ring correlation value of ξ calculated for peripheral pixels at different length scales. Red circles and curve show the mean across the 5 puff sites. Blue symbols and curve show corresponding ξ values at these puff sites before photorelease of i-IP_3. Error bars are ± 1SEM.

4.7. Spatial extent of correlations at active puff sites

Fluctuations arising from Ca^{2+} puffs are expected to be correlated across a distance scale corresponding to the spread of the Ca^{2+} fluorescence signal. To determine this distance, we calculate cross-correlations considering increasing square areas ($\ell x \ell$ pixels), around a given pixel where correlations are maximal. The fluorescence trace from the center pixel (gray dots in Fig. 6A) is cross-correlated with traces from peripheral neighboring pixels (red dots). ξ values for the center pixel at length scale ℓ are then calculated from the mean averaged cross correlation curve. Fig. 6B plots mean ξ values, averaged over 10 time subsections, as a function of increasing ℓ. The open gray symbols of Fig. 6B plot mean ξ values for the individual puff sites P1-P5 identified in both the CRM and the PSM. Sites with larger amplitude puffs (P3, P2) show larger correlations than sites with lower amplitude puffs (P1, P4). The mean correlation averaged over five puff sites (red dots in Fig. 6B) falls to about one-half over a length scale of $\ell \sim 15$ pixels; corresponding to a radial extent of about 2.5 µm from the center pixel.

4.8. The cross-correlation time constant characterizes puff kinetics

Under the simplifying assumption that the time course of puffs approximates an instantaneous rise and exponential fall [24], the correlation function will be an exponential with the same time constant as the puff decay. To estimate mean puff decay times we thus fit the correlation curves for puff sites with single exponentials as an alternative method to the spectral analysis in Fig. 4. After stripping slow changes in baseline fluorescence using the Matlab filter 'sgolayfilt', we calculated mean cross-correlations between each center pixel and the

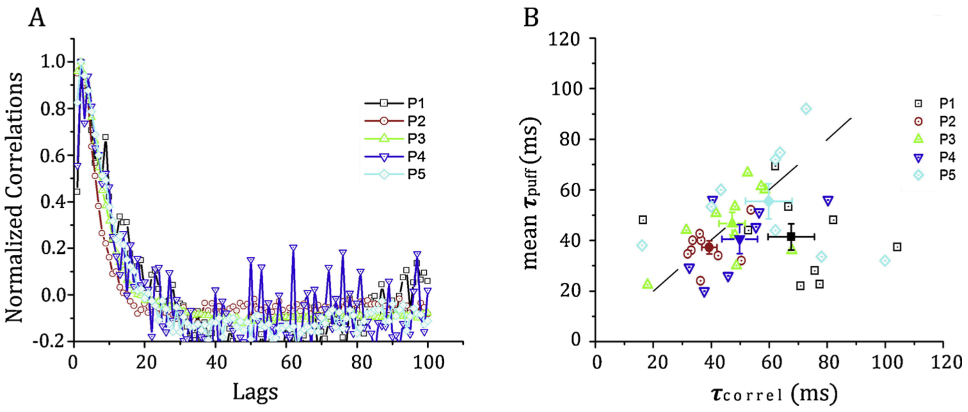

Fig. 7. Puff kinetics determined from cross-correlation analysis. (A) Mean cross correlation curves for each of the five puff sites in Fig. 5 (different symbols and colors), each derived from 15 × 15 pixel ROIs and averaged over ten 500 frame subsections. Data are plotted after normalizing each curve to the same maximum correlation. (B) Scatter plots of decay times of single exponential fits to correlation curves vs. puff decay times τ_{puff} measured directly from fluorescence traces as in Fig. 4. Each open symbol (n = 44) represents decay times from a single time subsection. Mean values for each puff site are shown by solid symbols with error bars denoting ± 1SEM. The dashed gray line represents a one-to-one correspondence.

surrounding 8 pixels within a 3 × 3 pixel region, and then averaged the values within a 15 × 15 pixel ROI centered on the puff site.

Fig. 7A shows mean cross correlation curves for 10 time sub-sections for the puff sites P1-P5 illustrated in Fig. 5. To aid visualization, the curves are normalized to the same peak amplitude. Fig. 7B shows a scatter plot of correlation curve decay times (x-axis), measured from single exponential fits to curves from individual time sub-sections from the five puff sites against the corresponding mean puff decay times measured directly from the fluorescence traces (y-axis). Mean values for each site are shown by solid symbols, and for most sites lie close to a one-to-one relationship (black dotted line), indicating that the cross-correlation analysis provides a good estimate of mean puff kinetics. The greatest deviation was observed for site P1 (black squares), which showed the lowest amplitude puffs and would thus be most susceptible to errors. Measurements from individual time subsections showed too much scatter to provide a useful measure.

4.9. Power spectra and correlations identify 'Ca^{2+} channel noise'

Flash photorelease of IP_3 in *Xenopus* oocytes at concentrations of several tens of nM evokes Ca^{2+} puffs and blips that are readily resolved as discrete events by linescan confocal and TIRF microscopy [25–29]. In freshly isolated oocytes, intracellular injections of much lower (picoMolar) concentrations of IP_3 evoke a different mode of Ca^{2+} release, evident as a small increase in baseline fluorescence without evident local, transient events [22]. This provides an interesting test case to apply power spectrum and correlation analysis to look for localized Ca^{2+} fluctuations in a situation where discrete events are not resolved.

Oocytes were loaded with fluo4-dextran (low affinity) and prepared for imaging as described in [22]. A micropipette containing 100 pM IP_3 was inserted through the oocyte and positioned with its tip towards the top of the imaging field and located a few μm inward from the cell membrane. Fig. 8 illustrates a representative experiment where Injecting IP_3 led to a fluorescence increase throughout the imaging field, but no localized Ca^{2+} elevations were detectable by eye. A long baseline was recorded (~ 5000 frames at 2 ms per frame) before a 10 nl bolus of IP_3 was injected into the cell, and a further 5000 frames were captured. The red and black traces in Fig. 8A show averaged fluorescence from fourteen 3 × 3 pixel ROIs. PSMs and CRMs were calculated for sub-sections before (baseline) and after (signal) times marked by the dotted lines above the traces.

The baseline mean PSM is shown in Fig. 8B. It is generally uniform, but a few isolated ROIs, at the top of the image, have higher power and stand out in comparison to their neighbors. These likely resulted from leakage of IP_3 from the pipette tip. Following intracellular injection of IP_3, several small localized regions exhibited increased power, signifying local release of Ca^{2+} from IP_3R's (Fig. 8C).

The maximum correlation maps showed a similar pattern. Compared to the baseline CRM (Fig. 8D), several regions stand out as strongly correlated following IP_3 injection in the signal CRM (Fig. 8E). As noted before, the resolution of the CRM is finer than the PSM, and regions of higher correlation coincide with regions of higher power in the PSM.

We infer the hot spots of higher power and correlation to be sites in the oocyte where fluorescence fluctuations are a signature of underlying local Ca^{2+} release triggered by IP_3 injection. From the maximum correlation map (Fig. 8E, following IP_3 injection) we placed 3 × 3 pixel ROIs over 'active' (mean $\xi \geq 0.4$) and 'inactive' sites (mean $\xi \leq 0.2$). Fluorescence traces from these sites are plotted separately in Fig. 8A (active sites in red and inactive sites in black). To elucidate the properties of active sites versus inactive sites we looked at their power spectra and correlation curves, pooling data from 42 active and 42 inactive ROIs from three experiments.

Fig. 9 shows the mean difference spectra calculated for active and inactive ROIs following injection of IP_3. Active sites showed a pronounced excess of low frequency power after IP_3 injection (red spectrum) as compared to inactive sites (black spectrum). The difference spectrum of active sites showed a cutoff frequency of 1.7 Hz, corresponding to an exponential process with time constant of ~90 ms

Fig. 10A shows averaged cross correlation curves for the active (red) and inactive sites (black), before (inset) and after intracellular IP_3 injection (main plot). Inactive sites did not show any appreciable correlation before or after IP_3 injection. Active sites showed a small correlation prior to IP_3 injection, which we again attribute to leak of IP_3 from the injection pipette, but a stronger correlation was apparent following IP_3 injection. Exponential fitting to the mean correlation curve for active sites in the presence of IP_3 gave a time constant of about 50 ms (25 lags). This correlation was apparent only over a very short distance scale (Fig. 10B). Ring correlations, derived as in Fig. 6, were present only at a length scale $\ell = 3$ pixels, implying a radial spread of correlated signal at active sites of only about 0.5 μm.

5. Discussion

We investigated the presence of local Ca^{2+} fluctuations in fluorescence imaging data using complementary statistical techniques of power spectrum and cross-correlation analysis. Our aim was to separate various noise sources inherent in fluorescence recordings (instrumental, photon and molecular), and to look in particular for 'channel noise' fluctuations arising from Ca^{2+} flux into the cytoplasm through transient openings of Ca^{2+}-permeable channels. A key basis for this discrimination is that local cytosolic Ca^{2+} transients typically have durations of several or tens of ms, and thus predominantly represent low frequency fluctuations, in contrast to photon shot noise and molecular fluctuations that have substantially uniform power across the bandwidth of our recordings. We show that both spectra and cross correlation approaches are effective in detecting, localizing and characterizing local Ca^{2+} puffs that involving release of Ca^{2+} from the

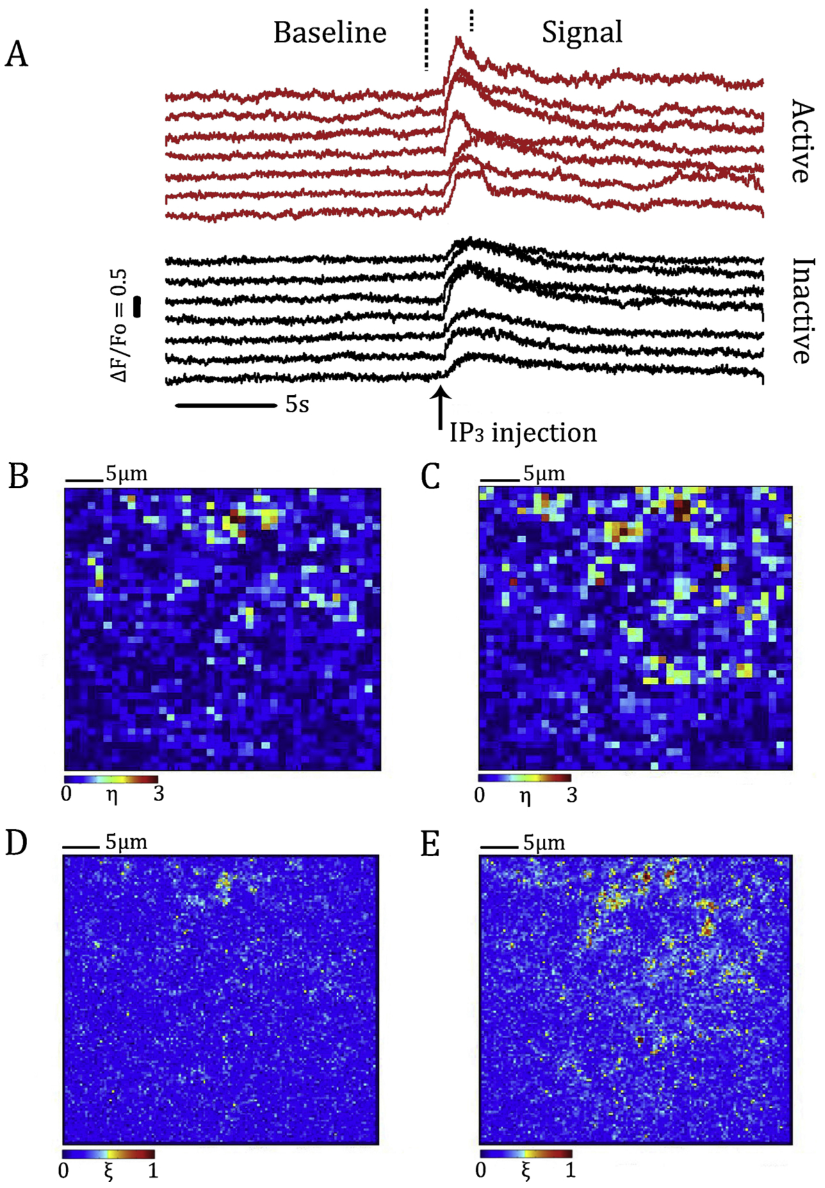

Fig. 8. Fluctuation analysis of Ca^{2+} signals evoked in *Xenopus* oocytes by picoMolar concentrations of IP_3 identifies hot spots of activity. (A) Mean fluorescence traces from 3 × 3 pixel ROIs, recorded before and after intracellular injection of 10 nl of 100 pM IP_3. Red traces are from 'active sites' that showed increased power and correlation post IP_3 injection. Black traces are from randomly selected 'inactive sites' where no increase in power or correlation was evident post IP_3 injection. (B, C) Mean PSMs derived, respectively, from 11 baseline sub-sections and 12 sub-sections following injection of IP_3. (D, E) Corresponding maximum CRMs before and after injection of IP_3.

concerted opening of a few clustered IP_3Rs [14,21]. Moreover these approaches hold promise for studying yet smaller local Ca^{2+} signals that cannot be readily resolved as discrete events in the raw fluorescence records.

5.1. Mapping of Ca^{2+} fluorescence fluctuations

Power spectra and correlation maps serve as visual tools, condensing fluorescence activity of a 3D image stack onto a 2D map, representing either the average or the maximal activity throughout an extended time period. Once hot-spots of activity are located, the spectra and cross correlation curves from these regions provide information on the average kinetics of the underlying events. A train of exponential pulses produces a Lorentzian power spectrum, with a cut-off frequency proportional to the exponential decay time constant, and an asymptotic power at low frequencies proportional to square of pulse amplitude and linearly proportional to pulse frequency. This situation is approximated by Ca^{2+} puffs, where the fluorescence signal generally shows a rapid rise and slower, roughly exponential fall [24]. Accordingly, we show that the cut-off frequencies of Lorentzian fits to power spectra from different puff sites correlate well with mean puff decay times measured directly from fluorescence traces at those sites. A caveat, however, is that measurements derived from power spectra will be strongly biased by those puffs with larger amplitudes, because the power (variance) increases with square of amplitude. For example, in a train of repeated puffs at a site, a puff of some given amplitude will contribute a power equivalent to four puffs of half that amplitude. Thus, estimates of mean puff decay times will be weighted by larger puffs in a train, and the strength of the excess power ratio η in the PSM will increase proportional to the square of puff amplitudes but only linearly in proportion to the frequency of puffs. The same considerations apply for maps and puff decay times derived from temporal cross-correlations between adjacent pixels.

Although power spectrum maps like those illustrated in Fig. 3 are effective in displaying regions of localized Ca^{2+} release, they are computationally slow to generate, and provide only poor time resolution because spectra are generated across time sections of hundreds of imaging frames. As a complementary approach, we have utilized the same concept of deriving a map showing regions exhibiting higher power (variance) at low frequencies, but rather than applying an FFT routine to calculate power spectra we instead directly calculate the temporal variance of each pixel within a running time window. This algorithm is implemented as a script running in the Python-based image-processing package FLIKA [30]. In brief, a fluorescence image

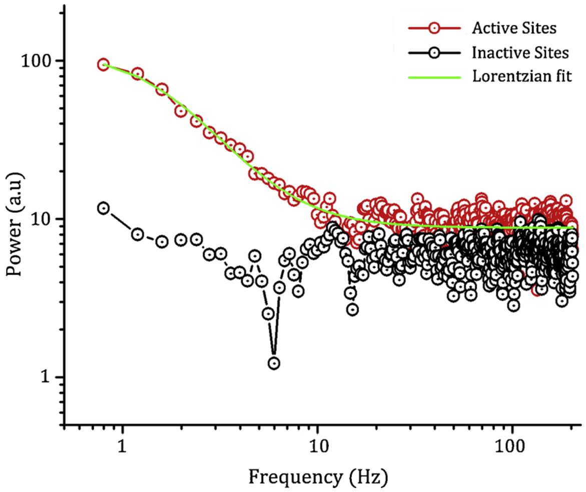

Fig. 9. Active sites show a marked increase in power following injection of 100 pM IP_3. Plot shows averaged difference spectra for ROIs placed on active (red) and inactive regions (black). Data are pooled from three experiments for a total of 42 active and 42 inactive sites. The green curve is a Lorentzian fit, rolling off to a noise floor at higher frequencies.

stack is temporally band-pass filtered to reduce high frequency shot noise and slow baseline drift, and a running boxcar function is then applied to calculate, pixel-by-pixel, the variance of the fluorescence signal around the mean. Finally, remaining shot noise variance is subtracted on the basis that this is linearly proportional to the mean fluorescence amplitude. With a fast PC the script processes image stacks at a speed only slightly slower than the speed typically used to initially acquire puff images, generating a variance movie that can be viewed in real time with a temporal resolution determined by the boxcar window.

5.2. The limits of detection

Existing software routines for locating and analyzing local transients in fluorescence images have employed an arbitrary detection threshold, which is typically set relative to the standard deviation of baseline fluorescence noise [30–32]. This method works well for brighter events, but reports many false positives if the threshold is lowered to match events that are close to baseline noise fluctuations. We expected that statistical analysis of ensemble activity at a site over time would improve upon this thresholding approach, analogous to the application of noise analysis to elucidate single-channel properties in voltage [18] and current [33] recordings that were too noisy to resolve individual channel events. To this end, we illustrate experiments where picoMolar concentrations of IP_3 were injected into oocytes, generating a widespread Ca^{2+} elevation lasting several seconds, but on which no discrete local Ca^{2+} events (blips or puffs) were apparent [22]. Remarkably though, calculated power and correlation maps highlight small localized regions, or 'active sites', about a micron in spread which we interpret as the presence of Ca^{2+} flux through channels (cf. Fig. 8).

Photon shot noise dominates the baseline noise in our recordings. Relative to this, inherent dark and readout noise generated by current generations of scientific camera (emCCD or sCMOS) are negligible, as are instrumental fluctuations in our imaging system that might arise from factors such as laser power and pointing instabilities. Molecular fluctuations arising from binding and dissociation of Ca^{2+} to fluorescent indicator molecules and their diffusion in and out of the imaging volume (point spread function) of the microscope will also contribute noise, even under steady-state conditions of constant mean $[Ca^{2+}]$ [10]. However, these processes are rapid and much briefer than the temporal resolution of our imaging ($<$ 500 fps). For example, Sigaut et al. [34] measured fluorescence of a solution containing Fluo-4 and EGTA from a confocal spot with effective volume of ~0.5 fl and observed appreciable autocorrelation only at microsecond timescales. Consistent with this, we found no difference in baseline noise spectra from oocytes loaded with Fluo-4 or with the Ca^{2+} insensitive dye calcein for comparable fluorescence emission intensities. Moreover, the variance of the fluorescence signals increased in linear proportion to the mean fluorescence (supplemental Fig. S1), as expected if the dominant noise source were photon shot noise.

How might we improve our resolution of single-channel Ca^{2+} signals? In our present approach, employing TIRF imaging of a freely-diffusible cytosolic Ca^{2+} indicator, the resolution is limited primarily by photon shot noise arising from basal fluorescence. Because of the Gaussian statistics of shot noise, the signal-to-noise ratio improves as a square root function of mean intensity (number of photons). However, possibilities for improvement by increasing the brightness of fluorescence imaged by the camera appear limited. TIRF imaging objectives maximize light collection, and modern cameras approach the physical limit of sensitivity of 100 % quantum efficiency with negligible inherent noise. Currently available Ca^{2+} indicator dyes such as Fluo-4 and Cal-520 already have excellent dynamic range with minimal Ca^{2+}-independent fluorescence, and the use of higher concentrations of indicator to yield a brighter signal is constrained by increased Ca^{2+} buffering that may disrupt the system under study, while increased fluorescence excitation may induce photodamage as well as faster bleaching. A promising alternative approach would involve tethering a fluorescent Ca^{2+} indicator – either a small organic dye or fluorescent protein based probe – to the channel of interest [35]. The signal resulting from Ca^{2+} flux through a channel would then be much smaller than for a freely diffusible probe in the cytosol, with only one or a few

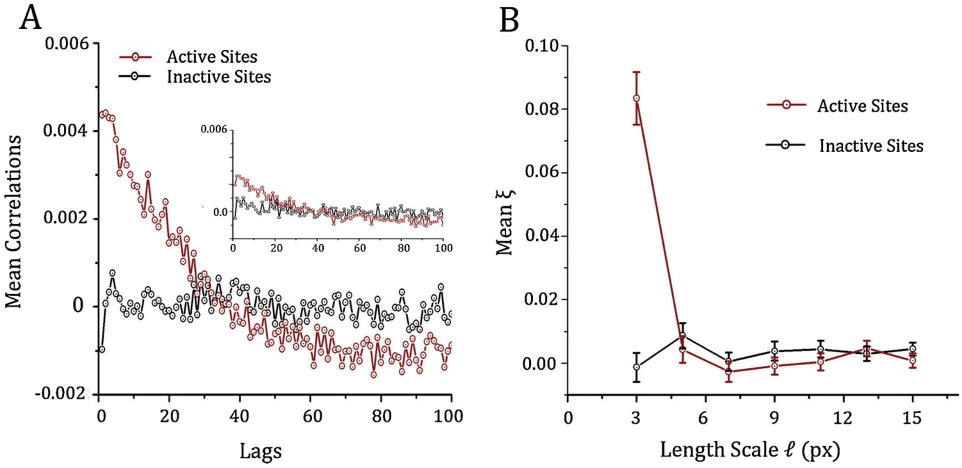

Fig. 10. Active sites show an increase in correlations following 100 pM IP_3 injection. (A) Averaged cross correlation curves for 42 active (red) and 42 inactive sites (black) following intracellular IP_3 injection. The inset shows cross correlation curves for baseline recordings at the same sites before IP_3 injection. Data points are means of pixel correlations across 42 3×3 pixel ROIs and 12 time sub-sections. (B) Mean ξ values (post injection of i-IP_3) as a function of increasing correlation length scale ℓ (pixels, 1 pixel = 0.333 μm) for the 42 active and inactive sites. Mean ξ values were calculated as in Fig. 6B. Error bars are ± 1SEM.

probe molecules per channel versus tens or hundreds of cytosolic probe molecules binding to Ca^{2+} ions liberated through the channel [10]. In compensation, noise arising from basal fluorescence may be reduced to a greater extent by selectively targeting the probe to minimize any free or non-specifically bound molecules and by further designing probes with very low Ca^{2+} affinity that responded only to the high concentration of Ca^{2+} in the immediate nanodomain around an open channel.

Author contributions

D.S. wrote software and performed all data analysis. A.D. and G.D.D. obtained experimental Ca^{2+} imaging data. I.P. initiated and directed the project. D.S. and I.P. wrote the manuscript. All authors have read and approved the published manuscript.

Declaration of Competing Interest

The authors declare they have no competing financial interests.

Acknowledgement

This work was supported by National Institutes of Health grants GM R37 048071 and GM RO1065830.

Appendix A. Supplementary data

Supplementary material related to this article can be found, in the online version, at doi:https://doi.org/10.1016/j.ceca.2019.102152.

References

[1] M.J. Berridge, P. Lipp, M.D. Bootman, The versatility and universality of calcium signalling, Nat. Rev. Mol. Cell Biol. 1 (2000) 11–21, https://doi.org/10.1038/35036035.

[2] M.J. Berridge, Annual review prize lecture. Elementary and global aspects of calcium signalling, J. Physiol. 499 (1997) 291–306.

[3] M.D. Stern, Buffering of calcium in the vicinity of a channel pore, Cell Calcium 13 (1992) 183–192, https://doi.org/10.1016/0143-4160(92)90046-U.

[4] S.L. Dargan, B. Schwaller, I. Parker, Spatiotemporal patterning of IP3-mediated Ca^{2+} signals in Xenopus oocytes by Ca^{2+}-binding proteins, J. Physiol. 556 (2004) 447–461, https://doi.org/10.1113/jphysiol.2003.059204.

[5] S.L. Dargan, I. Parker, Buffer kinetics shape the spatiotemporal patterns of IP3-evoked Ca2+ signals, J. Physiol. 553 (2003) 775–788, https://doi.org/10.1113/jphysiol.2003.054247.

[6] R. Filadi, T. Pozzan, Generation and functions of second messengers microdomains, Cell Calcium 58 (2015) 405–414, https://doi.org/10.1016/j.ceca.2015.03.007.

[7] E. Neher, Usefulness and limitations of linear approximations to the understanding of Ca++ signals, Cell Calcium 24 (1998) 345–357, https://doi.org/10.1016/S0143-4160(98)90058-6.

[8] M. Naraghi, E. Neher, Linearized buffered Ca2+ diffusion in microdomains and its implications for calculation of [Ca2+] at the mouth of a calcium channel, J. Neurosci. 17 (1997) 6961–6973 http://www.ncbi.nlm.nih.gov/pubmed/9278532.

[9] S.H. Weinberg, G.D. Smith, The influence of Ca2+ buffers on free [Ca2+] fluctuations and the effective volume of Ca2+ microdomains, Biophys. J. 106 (2014) 2693–2709, https://doi.org/10.1016/j.bpj.2014.04.045.

[10] J. Shuai, I. Parker, Optical single-channel recording by imaging Ca2+ flux through individual ion channels: theoretical considerations and limits to resolution, Cell Calcium 37 (2005) 283–299, https://doi.org/10.1016/j.ceca.2004.10.008.

[11] D. Toomre, D.J. Manstein, Lighting up the cell surface with evanes cent wave microscopy, Trends Cell Biol. 11 (2001) 298–303.

[12] A. Demuro, I. Parker, Imaging the activity and localization of single voltage-gated Ca(2+) channels by total internal reflection fluorescence microscopy, Biophys. J. 86 (2004) 3250–3259, https://doi.org/10.1016/S0006-3495(04)74373-8.

[13] A. Demuro, I. Parker, "Optical Patch-clamping", J. Gen. Physiol. 126 (2005) 179–192, https://doi.org/10.1085/jgp.200509331.

[14] I.F. Smith, I. Parker, Imaging the quantal substructure of single IP3R channel activity during Ca2+ puffs in intact mammalian cells, Proc. Natl. Acad. Sci. U. S. A. 106 (2009) 6404–6409, https://doi.org/10.1073/pnas.0810799106.

[15] I.F. Smith, S.M. Wiltgen, J. Shuai, I. Parker, Ca(2+) puffs originate from preestablished stable clusters of inositol trisphosphate receptors, Sci. Signal. 2 (2009), https://doi.org/10.1126/scisignal.2000466 ra77.

[16] S.M. Wiltgen, I.F. Smith, I. Parker, Superresolution localization of single functional IP3R channels utilizing Ca2+ flux as a readout, Biophys. J. 99 (2010) 437–446, https://doi.org/10.1016/j.bpj.2010.04.037.

[17] I. Parker, Y. Yao, Ca2+ transients associated with openings of inositol trisphosphate-gated channles in Xenopus oocytes, J. Physiol. 491 (1996) 663–668, https://doi.org/10.1113/jphysiol.1996.sp021247.

[18] B. Katz, R. Miledi, The statistical nature of the acetycholine potential and its molecular components, J. Physiol. 224 (1972) 665–699, https://doi.org/10.1113/jphysiol.1972.sp009918.

[19] L.J. DeFelice, Introduction to Membrane Noise, 1st ed., Springer, US, 1981, https://doi.org/10.1007/978-1-4613-3135-3.

[20] K. Feldbauer, D. Zimmermann, V. Pintschovius, J. Spitz, C. Bamann, E. Bamberg, Channelrhodopsin-2 is a leaky proton pump, Proc. Natl. Acad. Sci. U. S. A. 106 (2009) 12317–12322, https://doi.org/10.1073/pnas.0905852106.

[21] G.D. Dickinson, I. Parker, Factors determining the recruitment of inositol trisphosphate receptor channels during calcium puffs, Biophys. J. 105 (2013) 2474–2484, https://doi.org/10.1016/j.bpj.2013.10.028.

[22] A. Demuro, I. Parker, Picomolar sensitivity to inositol trisphosphate in Xenopus oocytes, Cell Calcium 58 (2015) 511–517, https://doi.org/10.1016/j.ceca.2015.08.003.

[23] G.D. Dickinson, D. Swaminathan, I. Parker, The probability of triggering calcium puffs is linearly related to the number of inositol trisphosphate receptors in a cluster, Biophys. J. 102 (2012) 1826–1836.

[24] S.M. Wiltgen, G.D. Dickinson, D. Swaminathan, I. Parker, Termination of calcium puffs and coupled closings of inositol trisphosphate receptor channels, Cell Calcium 56 (2014) 157–168, https://doi.org/10.1016/j.ceca.2014.06.005.

[25] I. Parker, I. Ivorra, Characteristics of membrane currents evoked by photoreleased inositol-trisphosphate in Xenopus oocytes, Am. J. Physiol. 263 (1992) C154–C165.

[26] Y. Yao, J. Choi, I. Parker, Quantal puffs of intracellular Ca2+ evoked by inositol trisphosphate in Xenopus oocytes, J. Physiol. 482 (1995) 533–553, https://doi.org/10.1113/jphysiol.1995.sp020538.

[27] I. Parker, J. Choi, Y. Yao, 1996_parker_choi_yao_88.pdf, Cell Calcium 20 (1996) 105–121, https://doi.org/10.1016/S0143-4160(96)90100-1.

[28] X.P. Sun, N. Callamaras, J.S. Marchant, I. Parker, A continuum of InsP3-mediated elementary Ca2+signalling events in Xenopus oocytes, J. Physiol. 509 (1998) 67–80, https://doi.org/10.1111/j.1469-7793.1998.067bo.x.

[29] H.J. Rose, S. Dargan, J. Shuai, I. Parker, "Trigger" events precede calcium puffs in Xenopus oocytes, Biophys. J. 91 (2006) 4024–4032, https://doi.org/10.1529/biophysj.106.088872.

[30] K.L. Ellefsen, B. Settle, I. Parker, I.F. Smith, An algorithm for automated detection, localization and measurement of local calcium signals from camera-based imaging, Cell Calcium 56 (2014) 147–156, https://doi.org/10.1016/j.ceca.2014.06.003.

[31] S.I. Shah, A. Demuro, D.O.D. Mak, I. Parker, J.E. Pearson, G. Ullah, TraceSpecks: a software for automated idealization of noisy patch-clamp and imaging data, Biophys. J. 115 (2018) 9–21, https://doi.org/10.1016/j.bpj.2018.06.003.

[32] S.I. Shah, M. Smith, D. Swaminathan, I. Parker, G. Ullah, A. Demuro, CellSpecks : a software for automated detection and analysis of calcium channels in live cells, Biophys. J. 114 (2018) 1–24, https://doi.org/10.1016/j.bpj.2017.11.1666.

[33] B.Y.C.R. Anderson, C.F. Stevens, Department of physiology and biophysics, University of Washington, J. Physiol. 235 (1973) 655–691.

[34] L. Sigaut, C. Villarruel, S.P. Dawson, FCS experiments to quantify Ca diffusion and its interaction with buffers FCS experiments to quantify Ca 2 + diffusion and its interaction with buffers, J. Chem. Phys. 146 (2017) 1–13, https://doi.org/10.1063/1.4977586 104203.

[35] J.L. Dynes, A. Amcheslavsky, M.D. Cahalan, Genetically targeted single-channel optical recording reveals multiple Orai1 gating states and oscillations in calcium influx, Proc. Natl. Acad. Sci. 113 (2016) 440–445, https://doi.org/10.1073/pnas.1523410113.